Journal Name

Pre-print submitted to Dalton Transactions 2015

Dynamic Article Links ►

Cite this: DOI: 10.1039/c0xx00000x

www.rsc.org/xxxxxx

ARTICLE TYPE

Complex magnetic behaviour of $Sr_2CoNb_{1-x}Ti_xO_6$ ($0 \le x \le 0.5$) as a result of a flexible microstructure

María Teresa Azcondo,*[a] Julio Romero de Paz[b], Khalid Boulahya[c], Clemens Ritter[d], Flaviano García-Alvarado[a] and Ulises Amador[a]

Received (in XXX, XXX) Xth XXXXXXXXX 20XX, Accepted Xth XXXXXXXXX 20XX
DOI: 10.1039/b000000x

We report the rich magnetic behaviour of $Sr_2CoNb_{1-x}Ti_xO_6$ ($0 \le x \le 0.5$) oxides as a result of their complex microstructure. Although these oxides show an average simple-cubic perovskite structure, they present a flexible microstructure due to short-range ordering between Co/Ti and Nb cations in the perovskite B-sites. The microstructure consists of double-cubic perovskite domains grown in a simple-cubic perovskite matrix. The size and number of the double-cubic perovskite domains decrease as the Ti content increases. As a result of aliovalent substitution of Nb^{5+} by Ti^{4+} in the parent Sr_2CoNbO_6 mixed-valence Co^{3+}/Co^{4+} oxides are obtained. A spin glass-like state has been observed at low temperatures for all the series, with freezing temperatures increasing with the Ti-content in the range 22 to 33 K. Furthermore, the x=0.3 and x=0.5 samples show non-interacting superparamagnetic particles-like dynamics, associated to relative high amounts Co^{4+}, with "blocking temperatures" of 13 and ~16 K, respectively. The complex magnetic behaviour of the title oxides seems to be connected with the clustering of magnetic Co^{3+} and the distribution of Co^{4+} as a result of the microstructure.

Introduction

Interest on perovskite-like oxides has persisted in last years due to their potential use for technological applications. The stability of many of them in oxidizing and reducing atmospheres at high temperatures and their high electronic and ionic conductivities make these compounds promising materials. Thus, they could be used as components of several electrochemical devices, in particular as electrodes, electrolytes and interconnectors for Solid Oxide Fuel Cells (SOFC). In an electrolyte ionic conductivity should dominate over electronic conduction, whereas for interconnectors and electrodes high electronic conductivity is required. For electrode applications, besides good electronic conduction an adequate catalytic activity is needed[1, 2]. Some perovskite-like oxides may display these properties since they simultaneously present cations with mixed oxidation states and anionic (oxygen) vacancies[3-7]. Among perovskites, those called "double perovskites" with general formula $A_2BB'O_6$ show a large variety of compositions and properties, related to the ability of the perovskite structure to accommodate different transition metal cations of different sizes and electronic structures[6]. In addition, partial substitutions of cations, either in the A- or the B-site give a huge number of possibilities, which include: the induction of cations mixed oxidation states[8-10], the creation of anionic vacancies,[10] the introduction of A-site vacancies[11], etc.

In particular, cobalt and niobium-based perovskites are extremely interesting due to their outstanding electrochemical properties which make them candidates for applications in SOFC[9, 12-14] and as ceramic membranes for high temperature oxygen separation[15]. Besides, these materials are also being investigated due to their interesting magnetic, dielectric and electrical properties[16-24].

From the magnetic point of view the behaviour of cobaltites is strongly affected by the ability of Co^{3+} (d^6) and Co^{4+} (d^5) to adopt different spin states, that is, low spin, LS, intermediate spin, IS and high spin, HS. Thus a broad range of total-spin quantum-number values, S, may be operating (from the diamagnetic LS-Co^{3+} (S=0) to the "more magnetic" HS-Co^{4+} (S= 5/2)). These spin states change depending on various factors such as the structure, the local microstructure, "chemical effects" such as inductive effect, temperature, pressure, etc[25].

We report herein the magnetic properties of a series of cobaltites with compositions $Sr_2CoNb_{1-x}Ti_xO_6$ ($0 \le x \le 0.5$) together with a detailed structural and microstructural study. The complex magnetic behaviour of these materials can be explained as a result of their flexible microstructure.

Results and Discussion

Average composition and structure

As determined by X-ray diffraction (XRD) and energy-dispersive X-ray spectroscopy (EDS) performed on c.a. 20 microcrystals in the transmission electron microscope, all the samples $Sr_2CoNb_{1-x}Ti_xO_{6-\delta}$ ($0 \le x \le 0.5$) are single phase and their compositions are close to the nominal ones within the experimental errors.

There is some controversy in the literature about the structure of the parent Sr_2CoNbO_6 and related compounds. In the earliest study on this oxide, and analogous Ba-containing compounds, a simple-cubic (S.G. Pm-3m) perovskite structure was reported[12]. Similar results were reported for the solid solution $SrCo_{1-x}Nb_xO_{3-\delta}$ in the whole compositional range ($0 \le x \le 1$) using XRD[15, 17]. However, electron diffraction for some members of this series revealed extra spots suggesting a tetragonal symmetry (unit cell: $a \approx a_p$, $c \approx 2a_p$) and short-range order phenomena[15]. This cell and symmetry has been reported for the entire series $Sr_2Fe_{1-x}Co_xNbO_6$ ($0 \le x \le 0.9$), though no structural details were given[26]. Recently, J. Bashir and R. Shaheen[16], using conventional X-ray diffraction data, reported for the parent (non-doped) Sr_2CoNbO_6 a structure model of tetragonal symmetry (S.G. I4/m) with the so-called diagonal cell ($a \approx \sqrt{2}a_p$, $c \approx 2a_p$).

On the other hand, our powder XRD data of the whole series $Sr_2CoNb_{1-x}Ti_xO_6$ ($0 \le x \le 0.5$) (not shown) can be fitted with the simple cubic perovskite model. To get more insight into the structure of these materials, in particular on the cation distribution and oxygen content, neutron powder diffraction (NPD) experiments were performed. The two members of the series with the highest Ti-contents, i. e. x=0.3 and 0.5, were selected as examples. The refined structural parameters are given in Table SI1. Figure 1 shows the graphic result of the fitting of NPD for $Sr_2CoNb_{0.5}Ti_{0.5}O_6$ to the model on Table SI1 (the corresponding figure for x=0.30 is presented as Figure SI1).

The average structure can be described as a simple cubic perovskite with no cationic ordering or octahedra tilting, in agreement with the tolerance factor close to unity. This parameter ranges from 0.989 to 0.999 for Ti-content ranging from x = 0 to x=0.50. Interestingly, the oxygen substructure seems to be complete for x=0.3, i.e. no anion vacancies exist in this member; in contrast, for x=0.5 the oxygen content is 5.942(2). This suggests that low degrees of substitution of Nb^{5+} by Ti^{4+} induces the oxidation of Co^{3+} to Co^{4+} as the only charge-compensating mechanism. However for higher levels of substitution a second mechanism operates and some oxygen vacancies are produced. The $Sr_2CoNb_{1-x}Ti_xO_6$ oxides can tolerate some oxygen sub-stoichiometry only for sufficient low content of Nb^{5+} which can be explained on the basis of the crystal-chemistry of the present cations. Indeed, it is well known that Nb^{5+} ions strongly tends to be six-fold coordinated[27, 28], whereas Ti^{4+} [29] and Co^{3+} (and Co^{4+} resulting as a consequence of oxidation of cobalt) show a more "flexible" co-ordination, with environments such as 4-fold tetrahedron or 5-fold square-pyramid[25]. So, to tolerate some oxygen vacancies the material must contain a minimum concentration of such "flexible" ions.

This is in agreement with the cobalt oxidation state determined by thermogravimetric analyses (TGA) and electron energy loss spectroscopy (EELS), which reaches a maximum for x=0.3 (see below).

Microstructure and short-range structure

All the samples $Sr_2CoNb_{1-x}Ti_xO_6$ ($0 \le x \le 0.5$) were studied by high resolution electron microscopy (HREM) along different zone axes in order to fully reconstruct the reciprocal/real space. HREM images taken along the [001] and [111] directions reveal apparently well-ordered materials. The optical Fourier transforms (FTs) performed on those HREM micrographs only show the

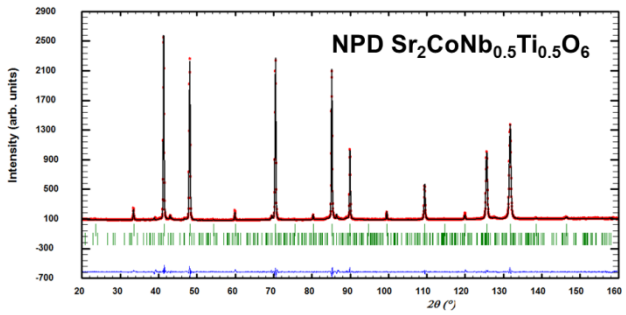

Fig. 1. Experimental (points), calculated (continuous line) NPD patterns and their difference (bottom) for $Sr_2CoNb_{0.5}Ti_{0.5}O_6$. The first row of vertical bars indicates the positions of Bragg peaks for this material; the second row corresponds to a small amount (c.a. 2% weight) of $Sr_7Nb_6O_{21}$.

maxima corresponding to the simple-cubic perovskite and therefore the whole crystal seems to be homogeneous, *i.e.*, there are not domains that could evidence the presence of additional ordering (see Electronic Supporting Information). However, in the case of the Sr_2CoNbO_6 oxide the HREM image along [1-10] direction, see Figure 2a, clearly reveals the presence of structural domains corresponding to a double-perovskite cell (labelled as A in Figure 2a) grown in a simple-cubic-perovskite matrix (labelled as B in Figure 2a). The optical FTs of the HREM images corresponding to the matrix and to the ordered domains are shown in Figure 2b and Figure 2c, respectively. In the later FT extra spots (such as ½(111)p indicated by an arrow in Figure 2c) are observed besides those spots corresponding to the simple cubic-perovskite which are the only ones observed in the former FT. The source of such extra spots may be the additional ordering of Nb^{5+} and Co^{3+} cations, the rotation or tilt of the corner-shared BO_6 octahedra that form the structure, or both effects simultaneously[30]. Due to the tolerance factor value (very close to unity) the amplitude of tilt is expected to be rather small and therefore the intensity of extra spots should be very weak. Hence, the intensity of the observed extra spots suggests the cationic ordering at octahedral sites as their main origin. In this sense, a similar short-range cationic ordering was reported for the similar compound Sr_2CoTaO_6[31]. The size of ordered domains (less than a hundred Å diameter) is clearly shorter than the coherence length of neutron or X-ray radiations, therefore no signal associated to this feature is observed in the NPD or XRD patterns. Thus, Sr_2CoNbO_6 oxide constitutes an interesting example of a perovskite oxide where, although order is not observed in the average structure, a microstructural study evidences the existence of short-range cationic ordering.

In the case of the samples $Sr_2CoNb_{1-x}Ti_xO_6$ with x= 0.1, 0.2 and 0.3, the HREM images along [110] direction show areas corresponding to a double perovskite like the sample with x= 0. For the sake of conciseness the HREM study of these samples is presented as Supporting Information (Figures SI2 to SI13). Interestingly, the increase of the Ti content induces a gradual growth of the simple-cubic-perovskite matrix and as a result for $Sr_2CoNb_{0.5}Ti_{0.5}O_6$ oxide homogeneous crystals are observed and the HREM image along [110] direction corresponds to a cubic-simple perovskite material, see Figure 3.

It is well established that the driven force for cation ordering in perovskites (either in the A-site or in the B-site) is the difference of charge and/or size[32]. In the parent Sr_2CoNbO_6 oxide Co^{3+} ions

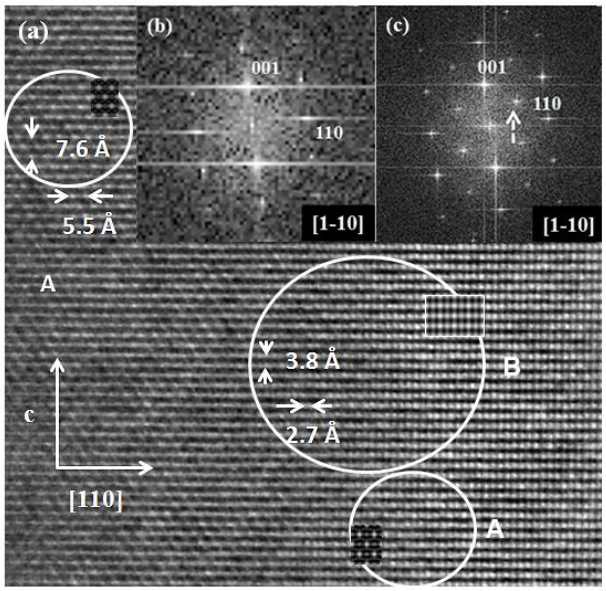

Fig. 2. (a) HREM image of Sr_2CoNbO_6 along [1-10]p. (b) and (c) optical FTs of disordered (labelled as B) and ordered (labelled as A) domains, respectively. Simulated images for both models are included.

($^{VI}r^{LS}$ = 0.55 Å) and Nb^{5+} ions (^{VI}r = 0.64 Å) have sufficient different charge and size to order, at least at short range. As Nb^{5+} is replaced by Ti^{4+} (^{VI}r = 0.605 Å) both charge and size differences between B-ions are reduced, as a result the ordered domains become smaller and less frequent. For these reasons, compositional differences may exist between the ordered and disordered domains. On the other hand, for high values of x, besides the oxidation of Co^{3+} as charge compensating mechanism for the aliovalent substitution of Nb^{5+} by Ti^{4+} a second mechanism operates and some oxygen vacancies are produced. On the basis of the crystal chemistry of Nb^{5+}, Co^{3+}, Co^{4+} and Ti^{4+} previously discussed[25, 27-29], it may be possible that the anion vacancies are associated to cobalt and titanium, in such a way that some compositional variation also in the oxygen content can be expected between the different domains observed by HREM.

Oxidation states

Physical properties of transition-metal oxides strongly depend on the metal oxidation state. Although in our case niobium, titanium and cobalt can present different oxidation states depending on the oxygen partial pressure and compound structure, by far cobalt shows the richest redox behaviour of these three elements. Of course, Nb^{5+} and Ti^{4+} can be also reduced, but relatively strong reducing conditions are needed (low pO_2 and high temperature).

Determining the oxidation state of cobalt helps to understand the properties of these materials. Two independent methods were used to do this: TGA and EELS spectroscopy. Table 1 collects the actual oxygen contents for the $Sr_2CoNb_{1-x}Ti_xO_6$ ($0\leq x\leq 0.5$) series as determined by TGA. For low Ti contents it seems that the main effect of the substitution of Nb^{5+} by Ti^{4+} is the oxidation of cobalt ions and hence almost no anionic vacancies would exist in the material. As x increases, the content of Co^{4+} reaches a maximum for x=0.3 and further substitution of Nb^{5+} by Ti^{4+} results in oxygen-vacancies creation.

This charge compensating scheme is in full agreement with what observed by NPD; indeed, the x=0.3 oxide is stoichiometric,

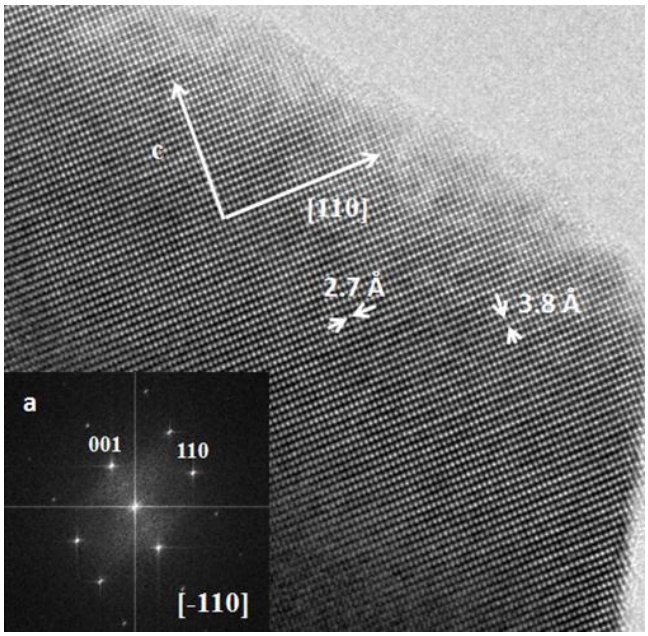

Fig. 3. HREM image of $Sr_2CoNb_{0.5}Ti_{0.5}O_6$ along [110]p. (a) Optical FT.

whereas for x=0.5 some concentration of oxygen vacancies has been detected (see Table SI1).

Table 1.Thermogravimetric analyses of $Sr_2CoNb_{1-x}Ti_xO_6$ ($0\leq x\leq 0.5$).

x nominal	Co^{4+}(±0.01)	Oxygen vacancies δ (±0.01)	Oxygen content (±0.01)
0.00	0.00	0.00	6.00
0.10	0.08	0.01	5.99
0.20	0.12	0.04	5.96
0.30	0.30	0.00	6.00
0.50	0.28	0.11	5.89

The formal oxidation state of cobalt for $Sr_2CoNb_{1-x}Ti_xO_6$ ($0\leq x\leq 0.5$) has been also determined by EELS. The study was performed by comparing the evolution of $Co(L_2,L_3)$ edges with x; the corresponding spectra are shown in Figure 4. They were normalized to the intensity of the L_3 maximum. For atoms such as Co one would expect the L_2/L_3 ratio to increase when the d band occupancy decreases, i.e. for increasing oxidation state[33].

The results show the Co oxidation state in Sr_2CoNbO_6 to be similar to that of the internal standard $Sr_2Co_2O_5$, containing only Co^{3+}. Thus, the analysis of the intensity ratio of the $Co(L_2/L_3)$ edges revealed all Co in Sr_2CoNbO_6 to be in the trivalent state, whereas both Co^{4+} and Co^{3+} are present in $Sr_2CoNb_{1-x}Ti_xO_6$ with $x\neq 0$. As Nb^{5+} is substituted by Ti^{4+} the EELS spectra presented in Figure 4 shows that the $Co(L_2/L_3)$ ratio increases suggesting the formal oxidation of cobalt ions as a result of the decrease of the Co d-band occupancy. At this point, it is important to emphasize that EELS result confirms that $Sr_2CoNb_{0.7}Ti_{0.3}O_6$ contains the maximum concentration of Co^{4+} (around 30%) since the $Co(L_2/L_3)$ intensity ratio does not change from x=0.3 to 0.5. It is worth noting the full agreement observed for Co^{4+} concentration and its evolution with x along the series $Sr_2CoNb_{1-x}Ti_xO_6$, determined by TGA and EELS.

The above results prove that Nb^{5+}/Ti^{4+} substitution in the $Sr_2CoNb_{1-x}Ti_xO_6$ system generates a mixed valence Co^{3+}/Co^{4+}

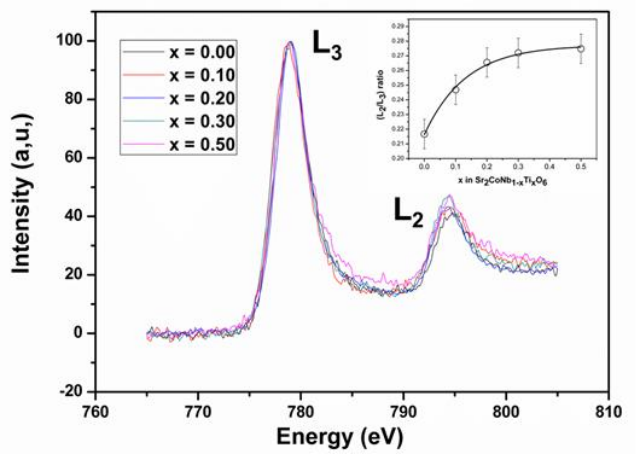

Fig. 4. EELS spectra of the Co(L_2,L_3) edges for 0.0 ≤ x ≤0.5 of $Sr_2CoNb_{1-x}Ti_xO_6$ compounds. Data have been normalized to the intensity of the L_3 maximum. The inset depicts the L_2/L_3 ratio as obtained from the corresponding integrated intensities.

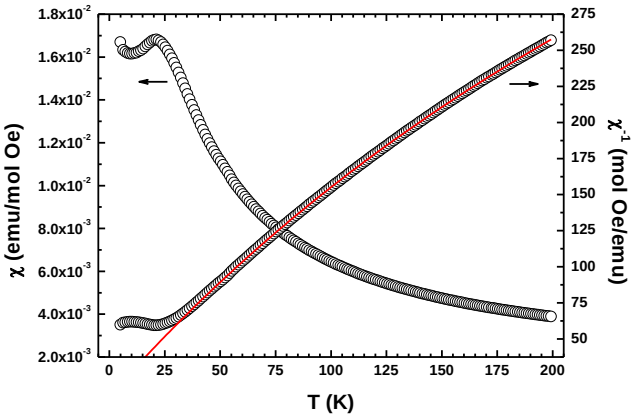

Fig. 5. Molar magnetic susceptibility and its inverse vs. temperature curves as measured in an applied field of 500 mT for $Sr_2CoNb_{0.9}Ti_{0.1}O_6$ oxide. The red solid line corresponds to the best fit (r^2= 0.99999) obtained using the χ= (C/(T-θ))+TIP function as indicated in the text.

system. Both, the Co^{4+} content and the microstructural details herein described are crucial to understand the magnetic properties of these oxides as discussed below.

Magnetic properties

The temperature dependence of molar magnetic susceptibility χ for the title samples shows a very different behaviour in two temperature regions: the first one from about 80 K up to RT, where a Curie-Weiss law (χ= (C/(T–θ)), being C and θ the Curie constant and the Weiss temperature, respectively) together with a temperature-independent paramagnetic contribution, TIP, is observed; the second one from 50 K down to 2 K, where magnetic interactions are operative resulting in the appearance of maxima in χ. As an example of such magnetism, Figure 5 depicts the temperature dependence of χ for $Sr_2CoNb_{0.9}Ti_{0.1}O_6$ oxide. In the next two subsections these results are discussed.

High temperature range: paramagnetic region

Table 2 collects the data obtained from the analysis of the temperature dependence of χ from RT to 80 K for the $Sr_2CoNb_{1-x}Ti_xO_6$ (0≤x≤0.5) series. In the case of the Sr_2CoNbO_6 oxide, the C and TIP parameters agree with those previously reported.[24, 34] The paramagnetism of this compound has two relevant features: a low value of C, and a high value of TIP. The origin of both features in the non-metallic Sr_2CoNbO_6 oxide can be unambiguously ascribed to the presence of a high amount of diamagnetic LS-Co^{3+}, which associated TIP value is around 1×10^{-3} emu mol^{-1} Oe^{-1} [35]. Thus, the experimental value of TIP points straightforward to the existence of a mixture of LS-Co^{3+} (S=0, with TIP contribution) and HS-Co^{3+} (S=2, with no TIP contribution) discarding a mixture of LS- and IS-Co^{3+} (S=1, with no TIP contribution) which will result in a much lower TIP value. From the experimental value of C c.a. 82% of the cobalt can be calculated as LS-Co^{3+} considering a theoretical spin-only value of 3.001 emu K mol^{-1} Oe^{-1} for the Curie constant of HS-Co^{3+}.

At this point, it is very interesting to compare the above paramagnetic parameters with those ones reported for the analogous compound Sr_2CoSbO_6[34, 36]. This oxide presents a larger magnetic moment value, 3.38 μ_B, and a smaller TIP, ~4×10^{-4} emu mol^{-1} Oe^{-1}. Such values denote the presence of a larger amount of magnetic Co^{3+} (IS and/or HS) and, suggest the weakening of the crystalline-field on Co^{3+} from the oxide ions as a result of the substitution of niobium by antimony. Since these two pentavalent cations have similar radii ($^{VI}r(Nb^{5+})$ = 0.64 Å, ($^{VI}r(Sb^{5+})$ = 0.61 Å)[32] we believe that the smaller electronegativity of Nb in comparison to that of Sb (Pauling electronegativities are: 1.6, 1.8 and 2.1 for Nb, Co and Sb, respectively)[37] increases the covalent character of Co–O bond in a Co–O–Nb arrangement and therefore favors the low-spin state of Co^{3+}. A similar effect on the stability of low-spin Co^{3+} by chemical substitution was observed in $LaCo_{1-x}M_xO_3$ oxides for M= Al, Ga and Rh[38]. In this connection, the substitution of Nb^{5+} by Ti^{4+} ($^{VI}r(Ti^{4+})$ = 0.605 Å[14]; Pauling electronegativity: 1.5[37]) in $Sr_2CoNb_{1-x}Ti_xO_6$ oxides is expected to have no further effect on the stabilization of non-magnetic Co^{3+} by the above described inductive effect since the Pauling electronegativities of Ti and Nb atoms are similar. However, that aliovalent substitution has an important effect on the spin-state of cobalt ions due to the particular microstructure, as discussed below. One can expect that in the title oxides magnetic Co^{3+} (experimenting a weak crystalline-field) will be surrounded mainly not by Nb/Ti but by a relative large number of other cobalt ions as second-neighbors; i.e. magnetic Co^{3+} ions will be located in a rich environment of O-Co^{3+} bonds. This is not possible when Co and Nb are ordered, i.e. inside the double-perovskite domains in which a -Nb-O-Co-O- sequence is produced as a result of the rock-salt ordering in the perovskite B-sites. On the contrary, in the simple cubic perovskite structure, a high degree of disorder of B-cations makes possible for a [CoO_6] octahedron to be surrounded by other [CoO_6] octahedra.

Coming back to Table 2, we can observe in the cases of $Sr_2CoNb_{1-x}Ti_xO_6$ oxides with x= 0.1, 0.2 and 0.3 that C increases and TIP decreases as x increases. Both trends of C and TIP can be explained considering the oxidation of diamagnetic LS-Co^{3+} to Co^{4+} as the main compensating mechanism of the aliovalent substitution of Nb^{5+} by Ti^{4+}. Thus, the increment of C can be mainly related with the amount of Co^{4+} present in the titanium substituted samples.

For x= 0.1 the slight increase of C (around 5%) is justified considering the presence of 7.4% LS-Co^{4+} (S= ½, spin only value of C= 0.374 emu K mol^{-1} Oe^{-1}, with no TIP contribution), a value

in good agreement with the amount of Co^{4+} (8±1%) determined

Table 2. Curie constant C, Weiss temperature θ and temperature-independent paramagnetism TIP values obtained by fitting the experimental dc magnetic susceptibility to the function $\chi = (C/(T-\theta))+TIP$ in the paramagnetic region (80-300 K). Magnetic moment μ values calculated as $\sqrt{8C}$ and amounts of low spin (LS) and high spin (HS) states for the cobalt ions calculated from the fitted C values as indicated in the text. Standard deviations are indicated in parenthesis.

Nominal Ti content	Co^{4+}/Co^{3+} (±0.01)[a]	C (emu K mol-1 Oe-1)	θ (K)	TIP (emu mol-1 Oe-1)	μ (μB)	Co^{3+} (%) LS	Co^{3+} (%) HS	Co^{4+} (%) LS	Co^{4+} (%) HS
x = 0	0.00/1.00	0.532(4)	−8.4(4)	1.65(1) ×10-3	2.06(1)	82	18	–	–
x = 0.1	0.08/0.92	0.560(2)	−5.8(2)	1.153(6) ×10-3	2.116(3)	74.6	18	7.4	–
x = 0.2	0.12/0.88	0.731(2)	−7.9(2)	7.35(7) ×10-4	2.418(3)	70	18	8.2	3.8
x = 0.3	0.30/0.70	1.198(4)	−7.3(2)	6(1) ×10-5	3.095(5)	52	18	16.2	13.8
x = 0.5	0.28/0.72	0.980(3)	−6.9(2)	8.36 ×10-4	2.800(4)	—[b]		—[b]	

[a] Co^{4+} values determined by TGA. [b] No value is calculated for x= 0.5 due to the formation of oxygen vacancies (see text).

by TGA measurements. It is worth noting that for other spin-states of Co^{4+}, either IS-Co^{4+} (S=3/2, spin only value of C= 1.872 emu K mol^{-1} Oe^{-1}) or HS-Co4+ (S=5/2, spin only value of C= 4.381 emu K mol^{-1} Oe^{-1}) the increment of C can be assigned to amounts of tetravalent cobalt much lower (1.5% or 0.6% for IS and HS, respectively) than that experimentally determined, 8%. However, for x= 0.2 the increment of C is no longer justified only with LS-Co^{4+}; a mixture of LS-Co^{4+} and HS-Co^{4+} seems to be more likely according to the spin state diagrams proposed by K.V. Lamonova et al[39]. Thus, the calculated percentages for such mixture of LS- and HS-Co^{4+}, taken 0.12 moles of Co^{4+} per formula unit, are 8.2 and 3.8, respectively, yielding a HS:LS ratio of 0.463. For x= 0.3 the large increasing of C discards the presence of LS-Co^{4+} alone and, in the same way that for x= 0.2, we propose a LS-HS mixture with percentages of 16.2 and 13.8, respectively (HS:LS ratio of 0.852), considering 0.3 moles of Co^{4+} per formula unit.

According to the effect of the second-neighbors electronegativity on the crystalline field in a given $Co^{4+}O_6$ octahedron, the low-spin and high-spin states will be favored for Ti/Nb-rich and Co-rich environments, respectively. As expected, the HS/LS ratio increases as the degree of substitution, *i.e.* the value of x, does. As observed by HREM this is a result of the microstructure evolution: for low values of x domains of double-ordered perovskite intergrow in a similar proportion with domains of simple-disordered perovskite, whereas for high Ti-contents ordered domains almost disappear.

Finally, for x= 0.5 the mentioned trend of C and TIP with x increasing is broken, probably due to the appearance of a second charge-compensating mechanism of substitution of Nb^{5+} by Ti^{4+}, the formation of oxygen vacancies, as inferred by TGA, EELS and NPD.

Low temperature region: glassy state

The temperature dependence of χ for $Sr_2CoNb_{0.90}Ti_{0.10}O_6$ is shown in Figure 5. As explained in what follows, the maximum observed at 21 K should not be associated with the onset of three-dimensional antiferromagnetic ordering. In this oxide the distribution of the magnetic units, which are dispersed in a diamagnetic matrix, hinders any kind of long-range magnetic order. Indeed, HS-Co^{3+} ions are located inside cobalt-rich domains (i.e. regions with high concentration of Co-O-Co sequences); whereas LS-Co^{4+} are likely isolated and located near Ti^{4+} ions.

Two alternative phenomena could account for the appearance of the aforementioned maximum. The first one is the onset of a frozen state of a spin glass, (with a characteristic frozen-temperature T_f) and the second one is the blocking of superparamagnetic particles (characteristic temperature T_B). In order to determine the origin of this maximum we carried out different magnetic measurements that we analyze below. Figure 6a shows the temperature dependence of the real part χ' and the imaginary part χ" of the ac magnetic susceptibility: the former presents a maximum at ~28.5 K whereas χ" suddenly increases at ~33 K. This points to the existence of relaxation processes in the material in this temperature region, but shed no light on their nature, *i.e.* both aforementioned phenomena would present a similar behaviour. Even more, from a qualitative point of view, the shift of the maximum in χ' to higher temperatures with increasing frequencies observed in Figure 6b, is also characteristic of these two kinds of materials. However, the shift, calculated by the expression $\Delta T_c(T_c)^{-1}[\Delta(\log \omega)]^{-1}$, (being T_c either T_f or T_B), is quantitatively different for these two cases[40]. Interestingly, the shift obtained for the x= 0.1 oxide is ~0.018, that falls within the range 0.004-0.080 expected for spin glasses[40], whereas the values expected for the blocking of non-interacting superparamagnetic particles would be in the range 0.1-0.3[40, 41].

Figure 7 shows the temperature dependence of zero-field-cooled magnetic susceptibility χ^{ZFC} and field-cooled magnetic susceptibility χ^{FC} in an applied magnetic field of 10 mT for x= 0.1 oxide. We observe that χ^{ZFC} and χ^{FC} are coincident down to ~35 K and then depart from each other below this temperature. Then, χ^{ZFC} shows a maximum around 26 K whereas χ^{FC} continuously increases down to 5 K, the lowest temperature reached. This is not the typical behaviour of a spin-glass material[40], since χ^{FC} should remain almost constant below 26 K. Worth noting, χ^{ZFC} shows at ~11 K a minimum that indicates the

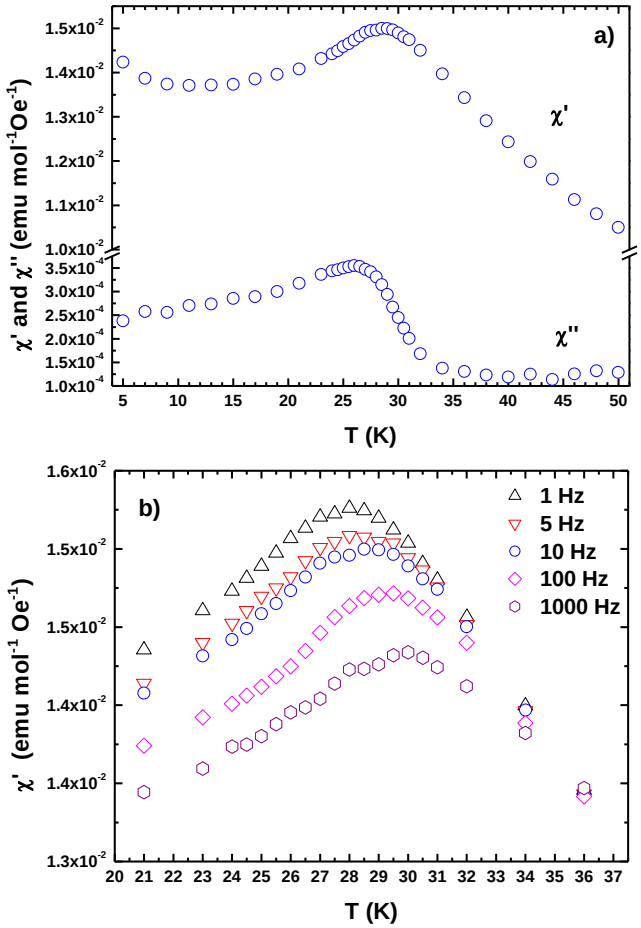

Fig. 6. a) Temperature dependence of the real part and imaginary part of the ac magnetic susceptibility for $Sr_2CoNb_{0.9}Ti_{0.1}O_6$ oxide measured at a driving field of 0.35 mT and 10 Hz. b) Frequency dependence of the real part measured at a driving field of 0.35 mT with frequencies 1, 5, 10, 100 and 1000Hz.

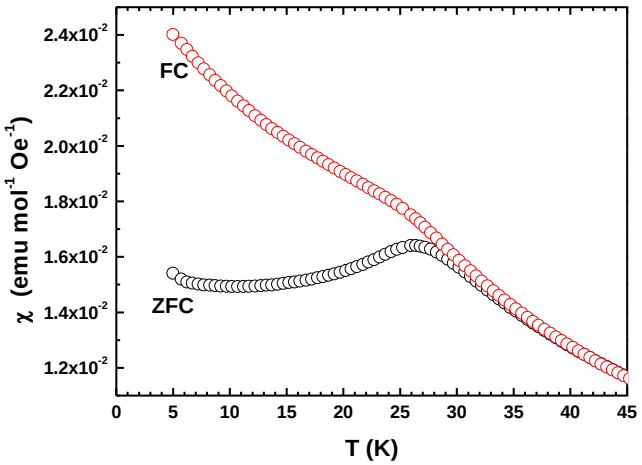

Fig. 7. Molar magnetic susceptibility vs. temperature curves for $Sr_2CoNb_{0.9}Ti_{0.1}O_6$ oxide as measured in an applied field of 10 mT following the zero-field cooled (ZFC) and field-cooled (FC) protocols.

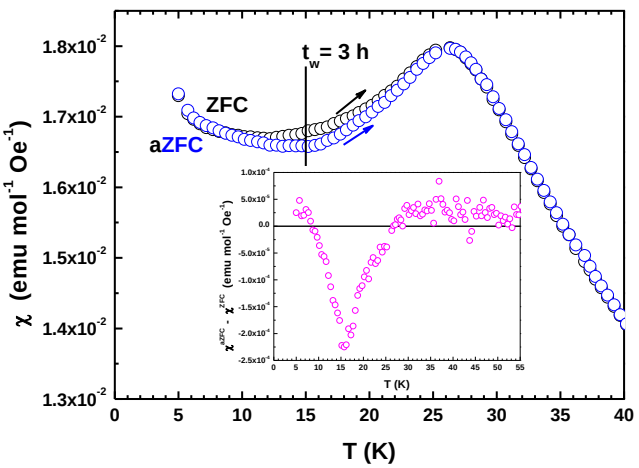

Fig. 8. Temperature dependence of aged χ^{ZFC}, obtained as indicated in the text, and not aged (normal) χ^{ZFC} measured in an applied field of 5 mT for $Sr_2CoNb_{0.9}Ti_{0.1}O_6$ oxide. The inset shows the temperature dependence of the aged χ^{ZFC} from not aged χ^{ZFC}.

presence of a second contribution, likely a paramagnetic one from isolated HS-Co^{3+} and/or LS-Co^{4+}, this could be the reason of the increasing of χ^{FC} below 26 K. The observed hump near 26 K in χ^{FC} supports this assertion.

With the aim of obtaining a clear signature of the low-temperature glassy-state, we investigated the existence of the so-called memory effect in χ^{ZFC} [42]. Thus, the sample was zero-field cooled from 150 K down to 15 K and it was left to age for 3 hours at this temperature. Then, the sample was cooled down to 5 K and, finally, the magnetization was measured in an applied magnetic field of 5 mT up to 100 K. Figure 8 shows how the sample "remembers" the stop as a broad dip around 15 K and the inset emphasizes the dip by the numerical difference between the aged χ^{ZFC} and the normal (without stop) χ^{ZFC}.

This result reflects a spin glass dynamics at low temperature for x= 0.1 oxide. A similar behaviour has been also found for the rest of the samples, which show different values of T_f. Thus, T_f increases from ~22 K for x= 0 to ~32 K for x= 0.5, with intermediate values of ~23, ~27 and ~29 K for x= 0.1, x= 0.2 and x= 0.3, respectively. All these values have been observed with an applied magnetic field of 100 mT. Since the parent oxide also show the described transition to a spin glass state, tetravalent cobalt ions seem to play no role in this behaviour. Thus, this spin glass-like behaviour is due to the clustering of the randomly positioned Co^{3+} ions and the superexchange interaction Co^{3+}–O–Co^{3+}. According to the Goodenough-Kanamori rules[43] this nearest-neighbour interaction is expected to be antiferromagnetic when two HS-Co^{3+} ions are involved or ferromagnetic when one HS-Co^{3+} ion and one LS-Co^{3+} ion are involved.

Finally, an extra maximum in χ at lower temperature is observed for the samples with x=0.3 and x=0.5, (see Figure 9). This second maximum is centered at 13 K for the former, whereas it actually appears as a shoulder around 16 K for the latter. The study of the nature of this second maximum has been done on the sample with x=0.3; corresponding data are given in the Figure SI 14.

The results are similar to those obtained for the first maximum, but the frequency shift of χ', evaluated through the expression $\Delta T_c(T_c)^{-1}[\Delta(\log \omega)]^{-1}$, takes a value of 0.143 which is in the range expected for non-interacting superparamagnetic particles (in contrast to 0.016 obtained for the first maximum). Furthermore, the memory effect on χ^{ZFC} at 6 K is very weak, (see Figure 10),

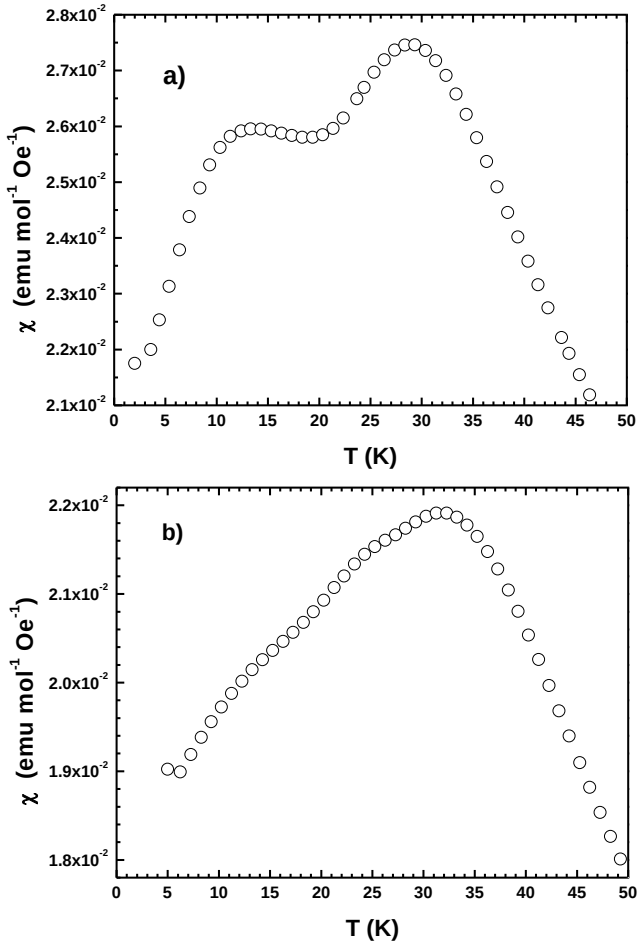

Fig. 9. Temperature dependence of dc χ at low temperature measured in an applied magnetic field of 100 mT for $Sr_2CoNb_{0.7}Ti_{0.3}O_6$ (a) and $Sr_2CoNb_{0.5}Ti_{0.5}O_6$ (b) oxides.

discarding magnetic interactions as the origin of the second maximum. Therefore, $Sr_2CoNb_{0.7}Ti_{0.3}O_6$ oxide presents a non-interacting superparamagnetic particles-like behaviour below 13 K that seems to be related with the presence of a sufficiently high amount of Co^{4+} in the material. Indeed, as stated above, this second maximum is only observed when the amount of Co^{4+} reaches its highest value, 0.30 moles per formula unit, furthermore, in two magnetic spin-states: low and high.

Experimental

Samples of compositions $Sr_2CoNb_{1-x}Ti_xO_6$ ($0 \leq x \leq 0.5$) were prepared by a modified Pechini method. Stoichiometric quantities of $Co(NO_3)_2.6H_2O$ (98% Aldrich), Nb_2O_5 (99.9% Aldrich) and $SrCO_3$ (99.9% Merck) were solved in water. A 5% excess of the stoichiometric Sr-content was used in order to compensate the volatility of SrO. Then, non-soluble high purity anatase (99.9% Aldrich) was added under stirring to obtain a homogeneous suspension. Citric acid was added under heating and vigorous stirring in a citric-acid-to-metal-ions molar ratio of 3:1. To promote polymerization ethylene glycol (5mL) was added yielding a viscous resin. This resin was decomposed by continuous heating and stirring until ashes were formed. The obtained powder was burned at 1073K to remove organic matter. After milling and homogenization the powders were pressed into

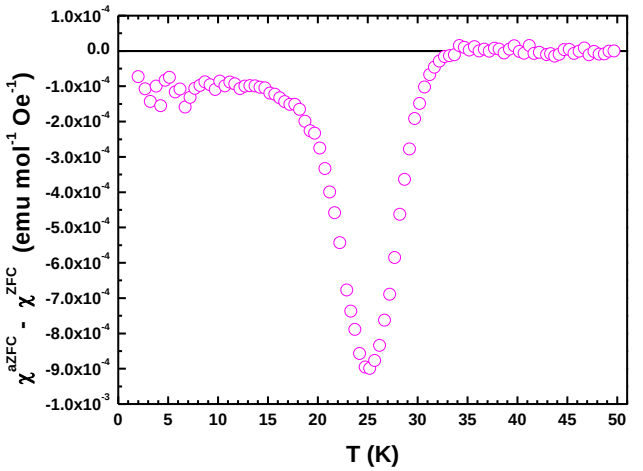

Fig. 10. Numerical difference between the aged χ^{ZFC} and the normal (without stop) χ^{ZFC} for $Sr_2CoNb_{0.7}Ti_{0.3}O_6$ oxide. The aging time was 3 hours, first at 23 K and then at 6 K.

13mm diameter pellets and fired at 1573K for 26h and cooled down to room temperature to obtain single-phase samples.

XRD patterns were recorded on a Bruker D8 high-resolution X-ray powder diffractometer, equipped with a LynxEye® position sensitive detector (PSD), using monochromatic CuKα (λ= 1.5406 Å) radiation obtained with a germanium primary monochromator. Data were collected in the range 2θ = 10-150º with a step width 0.015º (2θ) over a total exposure time period of 16 h.

NPD experiments at room temperature (RT) were performed on the high resolution diffractometer D2B at the Institut Laue-Langevin. A monochromatic beam of wavelength 1.5940 Å was selected with a Ge monochromator from the primary beam the divergence of which was defined by an additional 10' collimator to increase the instrumental resolution. The structural refinements were carried out by the Rietveld method by the simultaneous fitting of XRD and NPD data using FullProf program[44]. The neutron scattering amplitudes used in the refinement were 0.824, 0.702, 0.249, -0.344 and 0.581 (10^{-12}cm) for La, Sr, Co, Ti and O, respectively; isotropic thermal factors (ITF) were used for all atoms. Constraints employed throughout refinement involved considering the perovskite B sites fully occupied and adopting the same thermal factor for all oxygen atoms.

The cobalt oxidation state and oxygen content (assuming charge neutrality) of samples were determined by TGA using a D200 Cahn Balance. Typically, ca. 70 mg of the sample were weighed to a precision of ±0.0005 mg at a total reduced pressure of 400 mbar containing 60% He and 40% H_2. The sample was then heated to 1173 K at a rate of 2 K min^{-1}.

The samples were characterized by electron diffraction and high resolution electron microscopy (HREM) using a Jeol 3000 FEG electron microscope, fitted with a double tilting goniometer stage (±20°, ±20°) and operating at 300 kV. Simulated HREM images were calculated by the multislice method using the MacTempas software package. Local composition analyses by EDS and EELS spectra were obtained in the above mentioned microscope. EDS was performed using an Oxford analyzer system whereas for EELS measurements the microscope is equipped with Enfina EELS attachment. The energy resolution was better than 1 eV for all spectra as measured by the full-width

at half-maximum (FWHM) of the corresponding zero-loss peak. Both the background and plural scattering were subtracted from the experimental spectra to isolate the white-line intensities.

Magnetic measurements (either in dc or ac modes) were performed using a superconducting quantum interference device magnetometer (Quantum Design, model MPMS-XL). More details are given in the Magnetic Properties section for every kind of measurement performed. The diamagnetic contribution from each ion present in the materials was considered to analyse the experimental data[45].

Conclusions

The average structure of materials of the $Sr_2CoNb_{1-x}Ti_xO_6$ ($0 \leq x \leq 0.5$) series can be described as a simple cubic perovskite with no cationic ordering and no octahedra tilting, in agreement with the tolerance factor close to unity. However, HREM demonstrates that these materials present a complex microstructure with domains corresponding to a double-cubic-perovskite structure that intergrowth in a simple-cubic perovskite matrix. The size and the number of domains of double-perovskite (with rock-salt ordering of the B-ions) depend on the degree of substitution of Nb^{5+} by Ti^{4+}, i.e. the value of x: the higher the Ti content the smaller (and less frequent) the double-perovskite domains. This is a consequence of the weakening of the driven force for cation ordering: in the parent Sr_2CoNbO_6 oxide Co^{3+} ions ($^{VI}r^{LS} = 0.55$ Å) and Nb^{5+} ions ($^{VI}r = 0.64$ Å) have sufficient different charge and size to order whereas (at least at short range), as Nb^{5+} is replaced by Ti^{4+} ($^{VI}r = 0.605$ Å) the charge and size differences between B-ions decreases.

On the other hand, for high values of x, besides the oxidation of Co^{3+} as charge compensating mechanism for the aliovalent substitution of Nb^{5+} by Ti^{4+} a second charge compensating mechanism operates and some oxygen vacancies are produced. The $Sr_2CoNb_{1-x}Ti_xO_6$ oxides can tolerate some oxygen sub-stoichiometry only for sufficient low content of Nb^{5+} which can be explained on the basis of the crystal-chemistry of these ions. To tolerate some oxygen vacancies the material must contain a minimum concentration of Ti^{4+} and Co^{3+} (or Co^{4+}) ions which can adopt a variety of co-ordination with environments (4-, 5- and 6-fold) in contrast to Nb^{5+} ions which are always six-coordinated.

The magnetic behaviour of the title compounds is determined by the different magnetic species present and their distribution as a result of the microstructure. The parent compound contents a mixture of diamagnetic LS- (c.a.82%) and HS-Co^{3+} ions, these latter located in Co-rich domains with simple perovskite structure. Interestingly, this arrangement is not possible when Co and Nb are ordered, i.e. inside the double-perovskite domains in which -Nb-O-Co-O- sequence is produced as a result of the rock-salt ordering in the perovskite B-sites. However, in the simple cubic perovskite structure, a high degree of disorder of B-cations allows a given [CoO_6] octahedron to be surrounded by other [CoO_6] octahedra. By substituting Nb^{5+} by Ti^{4+} the order in the B-sites is progressively lost: the size and the amount of ordered domains decrease and for x=0.5 the material consists of a simple cubic disordered perovskite. As a consequence of the aliovalent substitution Co^{3+} is oxidized and the magnetic signal increases: for low levels of Ti content (x=0.1) only LS-Co^{4+} is present whereas a mixture of LS-Co^{4+} and HS-$Co^{4+}$is found for higher contents.

When cooled down, the title oxides present a spinglass-like dynamics with freezing temperatures increasing with the Ti content in the range 22 to 33 K. The origin of this glassy magnetic state seems to be in the clustering of magnetic HS-Co^{3+} dispersed in a diamagnetic matrix. On the other hand, the two members of the $Sr_2CoNb_{1-x}Ti_xO_6$ series with high Ti contents, i.e. x=0. 3 and 0.5, present a non-interacting superparamagnetic particles-like dynamics below 13 and 16 K, respectively. The origin of this second magnetic state is ascribed to a relatively large amount of Co^{4+} ions.

Acknowledgements

We thank the Ministerio de Economía y Competitividad (MINECO) and Comunidad de Madrid for funding the projects MAT2010-19837-C06, MAT2013-46452-C4-1-R and S2009/PPQ-1626, respectively. Financial support from Universidad San Pablo is also acknowledged. Access to the neutron facilities at the Institut Laue Langevin is gratefully acknowledged.

Notes and references

[a] *Departamento de Química, Facultad de Farmacia, Universidad CEU San Pablo Urb. Montepríncipe, Boadilla del Monte, E-28668, Madrid, Spain. Fax: 0034-91-3510496; Tel:; E-mail: azcondo@ceu.es*
[b] *CAI Técnicas Físicas , Facultad de Ciencias Físicas, Universidad Complutense de Madrid, E-28040, Madrid, Spain.*
[c] *Departamento de Química Inorgánica, Facultad de Ciencias Químicas, Universidad Complutense de Madrid, E-28040, Madrid, Spain.*
[d] *Institut Laue-Langevin, BP 156-38042 Grenoble Cedex 9, France.*

† Electronic Supplementary Information (ESI) available: **Figure SI 1.** Experimental and calculated NPD patterns for $Sr_2CoNb_{0.7}Ti_{0.3}O_6$. **Figure SI 2**. HREM image of Sr_2CoNbO_6 along [001]p and optical FT. **Figure SI 3.** HREM image of Sr_2CoNbO_6 along [111]p and optical FT. **Figure SI 4.** HREM image of $Sr_2CoNb_{0.9}Ti_{0.1}O_6$ along [001]p and optical FT. **Figure SI 5.** HREM image of $Sr_2CoNb_{0.9}Ti_{0.1}O_6$ along [111]p and optical FT. **Figure SI 6**. HREM image of $Sr_2CoNb_{0.9}Ti_{0.1}O_6$ along [110]p and optical FT. **Figure SI 7.** HREM image of $Sr_2CoNb_{0.9}Ti_{0.1}O_6$ along [110]p. Optical FTs corresponding to double-perovskite and simple-cubic perovskite domains. **Figure SI 8.** HREM image of $Sr_2CoNb_{0.8}Ti_{0.2}O_6$ along [001]p and optical FT. **Figure SI 9.** HREM image of $Sr_2CoNb_{0.8}Ti_{0.2}O_6$ along [111]p and optical FT. **Figure SI 10.** HREM image of $Sr_2CoNb_{0.8}Ti_{0.2}O_6$ along [110]p and optical FT corresponding to the superposition of ordered and disordered domains. **Figure SI 11.** HREM image of $Sr_2CoNb_{0.8}Ti_{0.2}O_6$ along [110]p. Optical FTs corresponding to double-perovskite domains and to simple-cubic perovskite domains. **Figure SI 12.** HREM image of $Sr_2CoNb_{0.7}Ti_{0.3}O_6$ along [1-10]p and optical FT. **Figure SI 13.** HREM image of $Sr_2CoNb_{0.7}Ti_{0.3}O_6$ along [110]p and optical FTs corresponding to double-perovskite domains and to simple-cubic perovskite domains. **Figure SI 14.** For $Sr_2CoNb_{0.7}Ti_{0.3}O_6$ oxide: a) Temperature dependence of real and imaginary parts of ac-χ; b) Temperature dependence of dc-χ measured following the ZFC and FC protocols; c) Frequency dependence of χ'; and d) Temperature dependence of aged χ^{ZFC} and not aged (normal) χ^{ZFC}.

1. Z. Liu, Han, M.-F., Miao, W.-T. , *J. Power Sources*, 2007, **173**, 837-841.
2. X. Sun, Wang, S., Wang, Z., Qian, J., Wen, T., Huang, F., *J. Power Sources*, 2009, **187**, 85-89.
3. S. B. Adler, *Chem. Rev*, 2004, **104**, 4791-4844.
4. J. W. Fergus, *J. Power Sources*, 2006, **162**, 55.
5. T. Ishihara, Ishikawa, S. , Ando, M. , Nishiguchi, H., Takita, Y. , *Solid State Ionics*, 2004, **173**, 9-15.

6. R. H. Mitchell, *Perovskite: Modern and Ancient*, Ontario (Canada), 2002.
7. N. Trofimenko, Ullmann, H., *Solid State Ionics*, 1999, **124**, 263-270.
8. A. Gómez-Pérez, Yuste, M.,Pérez-Flores, J.C.,Ritter, C., Azcondo, M.T., Canales-Vázquez, J., Gálvez-Sánchez, M.,Boulahya, K.,García-Alvarado, F., Amador, U., *Journal of Power Sources*, 2013, **227**, 309-317.
9. Z. Maupoey, Azcondo, M.T., Amador, U., Kuhn, A., Perez-Flores, J.C. , Romero de Paz, J., Bonanos, N. , Garcia-Alvarado, F. , *Journal of Materials Chemistry* 2012, **22**, 18033.
10. J. C. Pérez-Flores, Ritter, C., Pérez-Coll, D., Mather, G. C., Canales-Vázquez, J., Gálvez-Sánchez, M., García-Alvarado, F., Amador, U., *International Journal of Hydrogen Energy*, 2012, **37**, 7242-7251.
11. J. C. Pérez-Flores, Pérez-Coll, D., García-Martín, S., Ritter, C., Mather, G.C., Canales-Vázquez, J., Gálvez-Sánchez, M., García-Alvarado, F., Amador, U., *Chemistry of Materials*, 2013, **25**, 2484-2494.
12. Y. H. Huang, Liang, G., Craft, M. , Lehtimaki, M., Karppinen, M., Goodenough, J.B. , *Chem. Mater*, 2009, **21**, 2319.
13. S. J. Skinner, *Int. J. Inorg. Mater*, 2001, **3**, 113.
14. T. Xia, Li, Q., Meng, J., Cao, X. , *Mater. Chem. Phys*, 2008, **111**, 335.
15. V. V. Kharton, Yaremchenko, A.A., Kovalevsky, A.V., Viskup, A.P., Naumovich, E.N., Kerko, P.F. , *J. Membr. Sci*, 1999, **163**, 307.
16. J. Bashir, Shaheen, R. , *Solid State Sciences*, 2011, **13**, 993.
17. G. Blasse, *J. Appl. Phys*, 1965, **36**, 879.
18. J. W. G. Boss, Attfield, J.P. , *Phys. Rev. B*, 2004, **70**, 174434.
19. S. Ke, Fan, H., Huang, H. , *J. Electroceram.*, 2009, **22**, 252.
20. T. Motohashi, Caignaert, V., Pralong, V., Hervieu, M., Maignon, A., Raveau, B. , *Phys. Rev. B*, 2005, **71**, 214424.
21. E. L. Rautama, Caignaert, V., Boullay, Ph. , Kundu,A.K., Pralong, V., Karppinen, M., and C. Ritter, Raveau, B. , *Chem. Mater.*, 2009, **21**, 102.
22. S. Tao, Canales-Vazquez, J., Irvine, J.T.S., *Chem. Mater.*, 2009, **16**, 2309.
23. K. Yoshi, *J. Solid State Chem*, 2000, **151**, 294.
24. K. Yoshi, *J. Alloys and Compd.*, 2000, **307**, 119.
25. B. Raveau, Seikh, M. , *Cobalt Oxides: From Crystal Chemistry to Physics*, Wiley-VCH, Berlin, 2012.
26. J. W. Tian Xian, Nan Lin, Hui Zhao, Lihua Huo, Xueqiang Cao and J. Meng, *ECS Trans*, 2008, **13**, 207-215.
27. F. Lichtenberg, Herrnberger, A., Wiedenmann, K., Mannhart, J., *Prog Solid State Chem*, 2001, **29**, 1.
28. F. Lichtenberg, Herrnberger, A., Wiedenmann, K., *Prog Solid State Chem*, 2008, **36**, 253-387.
29. A. A. Osipov, Korinevskaya, G.G., Osipova, L.M., Muftakhov, V.A. , *Glass Physics and Chemistry*, 2012, **38**, 357-360.
30. D. I. Woodward and I. M. Reaney, *Acta Crystallographica Section B*, 2005, **61**, 387-399.
31. K. Boulahya, M. Parras and J. M. González-Calbet, *Chem. Eur. J.*, 2007, **13**, 910-915.
32. R. D. Shannon, *Acta Crystallogr., Sect. A*, 1976, **32**, 751.
33. S. J. Pennycook, Nellist, P.D. , ed., *Scanning Transmission Electron Microscopy Imaging and Analysis*, Springer Science+Business Media, New York, 2011.
34. Y. Kobayashi, Kamogawa, M., Terakado, Y., Asai, K., *J. Phys. Soc. Jpn.*, 2012, **81**, 044708.
35. B. N. Figgis and M. A. Hitchman, *Ligand Field Theory and Its Applications*, Wiley-VCH, New York, 2000.
36. Primo-Martín V. and M. Jansen, *J. Solid State Chem.*, 2001, **157**.
37. L. Pauling, *The Nature of the Chemical Bond* Cornell University Press, Ithaca, NY, 1960.
38. T. Kyômen, Asaka, Y., Itoh, M. , *Phys. Rev. B* 2003, **67**, 144424.
39. K. V. Lamonova, Zhitlukhina, E.S., Yu. Babkin, R., Orel, S.M., Ovchinnikov, S.G., Pashkevich,Y. G. , *J. Phys. Chem. A*, 2011, **115**, 13596.
40. J. A. Mydosh, *Spin Glasses: An experimental Introduction* Taylor and Francis, London, 1993.
41. J. l. Dormann, Bessais, L., Fiovani, D., *J.Phys.C: Solid State Physics*, 1988, **21**, 2015-2034.
42. M. Sasaki, Jönsson, P.E., Takayama, H., *Phys. Rev. B* 2005, **71**, 104405.
43. J. M. D. Coey, *Magnetism and magnetic materials*, Cambridge University Press, Cambridge (UK), 2010.
44. J. Rodríguez-Carvajal, *Physica B: Condensed Matter*, 1993, **192**, 55-69.
45. G. A. Bain, Berry, J.F., *J. Chem. Educ.*, 2008, **85**, 532.